



Published in final edited form as:

Virology. 1992 February ; 186(2): 655–668.

Cauliflower Mosaic Virus: A 420 Subunit ($T = 7$), Multilayer Structure

R. H. Cheng, N. H. Olson, and T. S. Baker

Department of Biological Sciences, Purdue University, West Lafayette, Indiana 47907

Abstract

The structures of the Cabb-B and CM 1841 strains of cauliflower mosaic virus (CaMV) have been solved to about 3 nm resolution from unstained, frozen-hydrated samples that were examined with low-irradiation cryo-electron microscopy and three-dimensional image reconstruction procedures. CaMV is highly susceptible to distortions. Spherical particles, with a maximum diameter of 53.8 nm, are composed of three concentric layers (I–III) of solvent-excluded density that surround a large, solvent-filled cavity (~27 nm dia.). The outermost layer (I) contains 72 capsomeric morphological units, with 12 pentavalent pentamers and 60 hexavalent hexamers for a total of 420 subunits (37–42 kDa each) arranged with $T = 7$ icosahedral symmetry. CaMV is the first example of a $T = 7$ virus that obeys the rules of stoichiometry proposed for isometric viruses by Caspar and Klug (1962, *Cold Spring Harb. Symp. Quant. Biol.* 27, 1–24), although the hexameric capsomers exhibit marked departure from the regular sixfold symmetry expected for a structure in which the capsid protein subunits are quasi-equivalently related. The double-stranded DNA genome is distributed in layers II and III along with a portion of the viral protein. The CaMV reconstructions are consistent with the model based on neutron diffraction studies (Kruse et al., 1987, *Virology* 159, 166–168) and, together, these structural models are discussed in relation to a replication-assembly model (Hull et al., 1987, *J. Cell Sci. (Suppl.)* 7, 213–229). Remarkable agreement between the reconstructions of CaMV Cabb-B and CM1841 suggests that other strains of CaMV adopt the Same basic Structure.

Introduction

Caulimoviruses comprise the first plant virus group whose genome was shown to be double-stranded DNA (dsDNA) (Shepherd et al., 1970). The type member, cauliflower mosaic virus (CaMV), has been extensively studied as a model system to understand genome organization, expression of viral genes, and replication strategy. More than 90% of freshly extracted CaMV dsDNA is present as a closed, nonsupercoiled circular molecule of about 8 kbp (~5000 kDa) (for reviews, see Hull et al., 1987; Mandahar, 1989). The complete genome sequences of three isolates of CaMV (Franck et al., 1980; Gardner et al., 1981; Bálazs et al., 1982) reveal eight open reading frames (ORF) that code for at least six gene protein (gp) products (gpl–gpVI) *in vivo* (Gordon et al., 1988; Maule et al., 1989). The presence of an efficient promoter in the genome sparked widespread interest in the use of

CaMV as a potential vector for introducing foreign genes into plants. Indeed, both bacterial (Brisson et al., 1984) and mammalian (Lefebvre et al., 1987; De Zoeten et al., 1989) gene products have been successfully expressed in recombinant CaMV genomes. The replication strategies of caulimoviruses are similar to animal viruses such as the retroviruses and hepatitis B virus (Hohn et al., 1985; Sanfaçon and Hohn, 1990).

Despite remarkable achievements in elucidating the organization and expression of the CaMV genome, the view, that “the basic physical structure of the virion remains largely unknown,” has persisted (Kruse et al., 1987). Observations of CaMV morphology by electron microscopy of purified samples prepared by conventional procedures such as metal-shadowing or negative-staining (e.g., Pirone et al., 1961; Itoh et al., 1969) led to a consensus view that CaMV virions are smooth, rather featureless spherical particles with an outer diameter of ~50 nm. Values reported for the CaMV diameter range from 35 to 45 nm for thin-sectioned (Fujisawa et al., 1967) or uranyl acetate-stained (Hills and Campbell, 1968) specimens and up to ~60 nm for metal-shadowed, air-dried samples (Pirone et al., 1961). Such variation can be accounted for by sectioning, decoration, or dehydration-induced artifacts inherent in the procedures used. In addition, despite much evidence that the composition and infectivity of CaMV is quite stable even in extreme conditions of pH, temperature, and chemical environment (e.g., Day and Venables, 1960; Itoh et al., 1969; Al Ani et al., 1979a), the morphology of CaMV seems to be more readily subject to distortion than that of most other viruses examined by similar procedures. The presence of capsomers in CaMV was first observed in samples disrupted by high pH, although no attempt was made to quantify the number of capsomers (Al Ani et al., 1979a).

Evidence that CaMV is hollow was obtained from observations that a “core” of ~20 nm diameter was accessible to potassium phosphotungstate stain in purified samples or remained unstained in thin-sectioned leaf tissue from infected plants (Fujisawa et al., 1967; Hills and Campbell, 1968; Rubio-Huertos et al., 1968). Subsequent studies, involving stepwise degradation of virions in the presence of pronase, led to the apparently contradictory suggestion that CaMV might be composed of several layers, including a central “core” similar to that in the small, structurally related (~50 nm dia. spherical viruses) papovaviruses, polyoma and SV40 (Tezuka and Taniguchi, 1972; Hull and Shepherd, 1976). The presence of a central, empty cavity (~25 nm dia.) was established by neutron diffraction experiments (Chauvin et al., 1979; Kruse et al., 1987) and later verified by direct observation of unstained, frozen-hydrated virions in the electron microscope (Cheng et al., 1989). The neutron diffraction results also provided compelling evidence that the protein and DNA in virions are distributed at low packing density in four concentric shells of different thickness and composition.

The DNA composition of CaMV virions is well established, but exact definition of the composition and stoichiometry of the protein components has remained elusive (e.g., Al Ani et al., 1979b; Maule et al., 1989). From the reported molecular mass of 22,800 kDa for the virion (Hull et al., 1976) and the calculated molecular mass (~5000 kDa) for CaMV DNA of known sequence (Franck et al., 1980; Bálazs et al., 1982), the protein is estimated to account for ~78% of the total virion mass, about the same reported by Kruse et al. (1987)

but smaller than the 83–84% values previously estimated by others (Hull et al., 1976; Chauvin et al., 1979).

The major capsid protein, gpIV, is translated *in vivo* from ORF IV as a 58-kDa precursor (Hahn and Shepherd, 1982) that is subsequently processed to several products, the major ones with apparent molecular masses of 37 and 42 kDa (e.g., Al Ani et al., 1979b). Evidence shows that gpIV in virions is glycosylated (e.g., Du Plessis and Smith, 1981) and phosphorylated (e.g., Hahn and Shepherd, 1980). Some gpIV may be present as disulfide-linked dimers (Al Ani et al., 1979b; Martínez-Izquierdo and Hohn, 1987). Virions are also believed to contain some gpIII (Giband et al., 1986; Mesnard et al., 1990) and gpV (e.g., Ménissier et al., 1984) as minor components.

On the basis of measurements of virion composition and the molecular weights of the virion components, various models have been proposed concerning the number and presumed icosahedral arrangement of protein subunits in the CaMV virion (Hull and Shepherd, 1976; Kruse et al., 1987). Estimates of the stoichiometry of the major coat protein (340–410 copies) have been subject to large errors, in part because of proteolysis of products of ORF IV and, in part because of large differences among various calculations of the virion molecular weight and the fractional amount of DNA present (e.g., Hull et al., 1976; Kruse et al., 1987). Even with these uncertainties, the overall dimensions of the virion and the probable number of copies of gpIV present argued in favor of a $T = 7$ icosahedral model for the virion shell, either with 420 copies of gpIV in a structure with quasi-equivalent subunit interactions (Caspar and Klug, 1962) or with 360 subunits arranged as in the papovaviruses (Baker et al., 1988, 1989, 1991). A $T = 1$ inner core (Hull and Shepherd, 1976), proposed from earlier observations of core-containing particles (Tezuka and Taniguchi, 1972), is unlikely given the compelling evidence for a hollow core (Kruse et al., 1987; Cheng et al., 1989).

Lack of definitive information about the organization of the DNA and protein components of CaMV prompted us to investigate the “native” structure of virions by cryo-electron microscopy and image analysis (Cheng et al., 1989). These procedures provide rigorous and objective means of recording images of biological specimens, whose morphology is well preserved in the microscope, and to reconstruct their three-dimensional structures (for review, see Stewart, 1990). We have determined the three-dimensional structure of CaMV from both severe (Cabb-B) and mild (CM 1841) strains. The two independent reconstructions, each computed to 2.5 nm resolution from low-irradiation images of unstained, frozen-hydrated samples, appear nearly identical and clearly establish a multilayer model for the organization of the nucleoprotein particles. Examination of these structures establishes the stoichiometry (420 copies) and arrangement ($T = 7$) of the major coat protein, and also provides a basis for understanding protein–DNA interactions, and the assembly and stability of the virions.

Materials and Methods

Virus samples

Purified samples of CaMV isolates Cabb-B and CM 1841 were kindly provided by Dr. R. J. Shepherd (University of Kentucky) who isolated and purified the virus according to the Triton-urea procedure (Hull et al., 1976). Samples of polyoma virus and reovirus (Type 1) were gifts from W. Murakami (Brandeis University) and D. Furlong (Harvard University), respectively.

Cryo-electron microscopy

We prepared frozen-hydrated specimens by applying 2.5- μ l droplets of an aqueous mixture containing CaMV (0.5–1.0 mg/ml) and polyoma virus or reovirus to holey carbon films on 400 mesh copper grids. Cryo-electron microscopy was performed with established procedures (Dubochet et al., 1988) with a Philips EM420 (Philips Electronics Instruments, Mahwah, NJ) operated at 80kV. Focal pairs of images were recorded with minimal exposure conditions (1000–2000 $e^-/\text{nm}^2/\text{image}$) on Kodak SO-163 film (Eastman Kodak Co., NY) at nominal magnifications of 49,000 \times for Cabb-B and 36,000 \times for CM 1841. The first (lowest total dose) image in each focal pair was generally recorded 1.2–1.5 μ m underfocus. The second micrograph was recorded an additional \sim 1.2 μ m underfocus to further enhance phase contrast (Erickson and Klug, 1971; Stewart and Vigers, 1986). Polyoma served as an internal magnification standard for measuring CaMV particle dimensions (Olson and Baker, 1989; Cheng et al., 1989).

Image analysis and three-dimensional reconstruction

Micrographs exhibiting minimal astigmatism and specimen drift were digitized at 25- μ m intervals (corresponding to \sim 0.5 or \sim 0.7 nm sampling at the specimen) on a rotating-drum microdensitometer (Optronics Model C-4100, Optronics International Inc., Chelmsford, MA). We calibrated image magnification with cross-correlation procedures (Olson and Baker, 1989) and radial density fitting (Steven et al., 1984; Belnap, Olson, and Baker, unpublished results). Images of frozen-hydrated CaMV samples were analyzed with established icosahedral particle processing procedures (e.g., Crowther et al., 1970; Fuller, 1987; Baker et al., 1988) to reconstruct the three-dimensional structures of the viruses in a manner similar to that used to study SV40 (Baker et al., 1989) and bovine and human papilloma viruses (Baker et al., 1991). Images of particles that appeared distorted or degraded, or in regions where the vitreous sample was too thick, were rejected. Computations were performed with interactive FORTRAN programs on VAXA/MS 11/750 and 8550 minicomputers (Digital Equipment Co., Maynard, MA) and images were displayed with a 1280 \times 1024 pixel raster graphics device (Baker et al., 1991).

The more defocused micrograph of a focal pair was processed first because the stronger phase contrast in it enabled us to determine initial estimates of individual particle orientations. Initial estimates of particle centers (phase origins) were obtained by use of a cross-correlation method (Olson and Baker, 1989) and modified common-lines procedures (Fuller, 1987; Baker et al., 1988). This was followed by inter-particle orientation refinement of increasing numbers of unique images with cross-common-lines procedures (Fuller, 1987).

To improve the sensitivity and reliability of the orientation refinement procedures with the very noisy CaMV images, we had to use data that were Fourier-filtered (e.g., Yeager et al., 1990) to remove both low ($<(1/12.8) \text{ nm}^{-1}$) and high ($>(1/3.4) \text{ nm}^{-1}$) frequency noise. Refinement of origins and orientations was repeated in cycles at progressively higher spatial frequencies until no further improvement was found in the common-line phase residuals. Refinement at a particular resolution was considered complete if the particle origins and orientations remained stable to within $\sim 0.1 \text{ nm}$ and 0.5 degree, respectively. The refined data were combined to produce a three-dimensional Fourier transform, and preliminary three-dimensional electron density maps were computed by use of the inverse Fourier-Bessel method (Crowther, 1971) to a resolution of 3.4 nm . This resolution is within the limit imposed by the first zero of the contrast transfer function of the electron microscope (this was also true for the final, higher resolution reconstructions, computed from less-defocused images, as described below). Back-projected images of the preliminary reconstruction were used as references to accurately refine the phase origins of the corresponding images from the digitized micrograph (Baker et al., 1990), and additional cycles of refinement were carried out as described above.

Phase origins of images of CaMV particles in the first (closer-to-focus, lower-total-dose) micrographs from the respective focal pairs were located by cross-correlating each particle image with its corresponding mate in the second (higher defocus, higher dose) micrograph. The orientation for each particle was initially set equal to the orientation that was determined for the corresponding particle image from the second micrograph. The new set of particle origins and orientations were first refined with data out to a resolution of $\sim 3 \text{ nm}$. Several intermediate three-dimensional reconstructions were calculated during the refinement process in order to periodically check particle origins by use of cross-correlation procedures as was done with the highly defocused data set. Refinement was carried out in several stages at progressively higher resolution out to $\sim(1/2.4) \text{ nm}^{-1}$.

On the basis of cross-common-lines phase residuals (Fuller, 1987), the best 21 (out of 44) Cabb-B images and 40 (out of 137) CM 1841 images from the closer-to-focus micrographs were separately combined to compute reconstructions to 2.5 nm resolution. We assessed the reliability of the reconstructions quantitatively and qualitatively: a reliability index, R_{AB} (Winkelmann et al., 1991), was computed between partial data sets within each strain and between the full data sets for both strains; features such as the size and location of capsomer subunits between reconstructions were compared directly. Because of the relatively featureless images of unstained CaMV and the high noise level of the low-irradiation images, it was not possible for us to assess the correctness of the reconstruction by visually comparing individual particle images with corresponding back-projected views of the reconstruction as has been done before (e.g., Baker et al., 1989; Yeager et al., 1990). We enforced full (532) icosahedral point group symmetry on the final reconstructed density maps by imposing threefold symmetry in real space (Fuller, 1987). Projections of the density contained within defined spherical shells were calculated by summing only those density points along chosen view directions that were within specified radii limits. Radial density profiles were computed by spherically averaging the three-dimensional reconstruction of the particle about its center at 0.5-nm intervals.

The reconstructions displayed in this report have not been corrected for the effects introduced by the contrast transfer function of the electron microscope (e.g., Erickson and Klug, 1971; Toyoshima and Unwin, 1988). Several attempts to apply such corrections in an objective way led to variable results. The main differences between those results and the ones reported here arose from the larger influence of the lowest resolution features in the compensated data. This deemphasizes the pronounced separation of the virion into a multilayer structure and also renders the higher resolution details, such as the subunit separation within capsomers, less distinct. However, the major features of the organization and structure of CaMV remain the same for both corrected and uncorrected data.

Results

Electron microscopy

Unstained, frozen-hydrated CaMV virions (Fig. 1) have circular profiles and markedly less dense centers compared to polyoma (Fig. 1C, arrow), a virus of similar size and total mass. The circular profiles of both viruses (presumed to be randomly oriented in the vitrified sample) indicate that the particles have approximately spherical morphologies. Although the sizes of both viruses appear virtually identical by the eye, CaMV has a slightly larger measured diameter than polyoma (53.8 nm vs 49.5 nm). Aside from obvious features such as the circular profile and hollow appearance, the three-dimensional structure of CaMV is difficult to interpret directly from the projected images since the images do not reveal characteristic superposition patterns as are common for the papovaviruses (Baker et al., 1989). With polyoma, some of the 72 capsomers, especially those near the edge, are clearly seen (Fig. 1C, arrow) and the characteristic superposition patterns of the virions allow some particle orientations to be directly identified (Baker et al., 1989). Although fine details can be discerned in CaMV images (Figs. 1B and 1C), none of the projected images are distinctive enough to allow specific orientations to be identified.

Whereas spherical viruses generally appear to be well preserved by cryo-microscopy procedures (Olson and Baker, 1989), CaMV undergoes substantial distortion during most conventional and cryo-electron microscopy preparation procedures. Many virions appear slightly ovoid in vitrified samples (Fig. 2), and close inspection of most CaMV images reveals a variety of deviations from perfect circular symmetry. Attempts to stabilize the virion structure with chemical fixation procedures (e.g., glutaraldehyde or uranyl acetate) were not successful. Distortion also did not seem to correlate with the age or purity of the CaMV samples or with significantly different purification protocols. CaMV seems to be slightly better preserved in thicker regions of vitrified samples (Fig. 2) indicating that interactions of CaMV with the air-water interface may influence virion morphology. The diameter of CaMV changes by up to 30% depending on the sample thickness (Fig. 2). We could not reproducibly control specimen thickness and obtain undistorted CaMV particles, and therefore we think only a narrow range of ice thicknesses may be adequate for optimal specimen preservation. Thus, even though CaMV is known to be chemically quite stable, it appears to have a rather flexible, easily distorted structure.

Image analysis

Images of CaMV were recorded as focal pairs (e.g., Figs. 1B and 1C) to facilitate the image processing necessary for computing a three-dimensional reconstruction from very noisy data. The first, low-dose image of each focal pair was recorded 1.2–1.5- μm underfocus, and this was immediately followed by a second image recorded at 2.4–2.7- μm underfocus. The strong contrast of the low resolution features in the high dose data (second image in each pair) enabled rough estimates of individual particle orientations to be determined and then refined. The orientations obtained in this way were then applied to the noisier (lower contrast, lower dose) data and refined. Data from the second micrograph were only used to help initiate refinement of the lower dose data and were not merged with these data as has been done to compute three-dimensional reconstructions of some viruses (e.g., Vogel et al., 1986; Fuller, 1987).

Representative Fourier transforms, computed from a focal pair of images of a single CaMV particle, and corresponding plots of the microscope contrast transfer functions for the two defocus levels used, are shown in Fig. 3. The use of transform data only within restricted resolution limits helped improve the refinement of particle center positions and orientations. By discarding the lowest spatial frequency data (mainly from circularly symmetric features) and highest spatial frequency data (mainly noise), we emphasized the icosahedrally symmetric components of the images and this markedly optimized refinement of particle view orientations. In computing the final CaMV three-dimensional reconstructions, all transform data (only from the low-dose images) between spatial frequencies of 0.0 and 0.4 nm^{-1} were used.

CaMV three-dimensional structure

A total of 21 images of Cabb-B and 40 images of CM1841 were included in the two final three-dimensional reconstructions computed to 2.5-nm resolution (Figs. 4A and 4B). The surface structures of both viruses are remarkably similar. The outer capsids each consist of 72 capsomers arranged with $T = 7$ icosahedral lattice symmetry (Fig. 4D), with 12 capsomers in pentavalent positions (where one capsomer is surrounded by five others) and the remaining 60 in hexavalent positions (where one capsomer is surrounded by six others). The measured diameters of the pentavalent and hexavalent capsomers are 8.3 and 10.3 nm in diameter, respectively, and both protrude ~ 3.6 nm above the base of the capsid surface. The hexavalent capsomers have a small but distinct axial hole (~ 1 nm diameter) not seen in the pentavalent capsomers. The capsid surface is punctuated by 140 large, triangular-shaped holes (~ 3 nm on a side) which occur at the 20 strict and 120 quasi-three-fold axes that relate groups of three capsomers. The handedness of the reconstructed density maps was arbitrarily computed with $T = 7 /$ (left-handed) icosahedral lattice symmetry, although the actual CaMV structure may be the other enantiomorph since the correct hand cannot be determined from a single field of view of particles. Attempts to determine the actual hand of the structure by metal shadowing or tilting experiments were inconclusive (R. H. Cheng, unpublished). Cross-sectional views of CaMV clearly reveal a prominent, empty center (Fig. 4C) with a diameter of ~ 27 nm. This view also reveals that CaMV has a rather open structure with density mainly confined between radii of 14.5 and 26.9 nm in three concentric layers (I, II, and III). The overall thicknesses of layers I, II, and III, starting with the outermost layer (I),

are about 5.7, 3.6, and 3.6 nm. The total volume of the virion, excluding only the solvent on the outside² surface, is $\sim 64,000 \text{ nm}^3$. The hollow center accounts for $\sim 12,500 \text{ nm}^3$ or 14% of the total virion volume.

A plot of the average radial density for the Cabb-B and CM1841 reconstructions clearly reveals the multilayer nature of CaMV (Fig. 5). Major peaks of density at radii of 23.5, 19.1, and 16.0 nm correspond to the densest regions of the three prominent layers. The small shoulder at $r = 12.9 \text{ nm}$ corresponds to some extra density at the boundary between the inner wall of the virion and the empty center. Negative peaks at $r = 26.9$ and 10.9 nm represent Fresnel fringes that are generated by the strong-defocus phase contrast and are most noticeable in regions of high contrast where there are large mass density differences (e.g., at virion-solvent boundaries). Density at $r < 10.9 \text{ nm}$ mainly corresponds to the solvent-filled central cavity. Ripples in the averaged density in this region occur with amplitudes that are approximately at the level of noise in the data and they are accentuated by defocus phase contrast and Fourier truncation artifacts. The residual positive density at radii $< 10.9 \text{ nm}$ may represent density contributed by variable amounts of molecules trapped inside the virion during the process of assembly (Discussion). The large negative peak at the center of the virion ($r = 0\text{--}2 \text{ nm}$) is mainly produced by noise in the data, which tends to build up nearest symmetry axes or where they intersect, and is caused in part by the Fourier-Bessel procedures used to reconstruct the density map.

The overall agreement between the Cabb-B and CM1841 data and the quality of the reconstructions were quantitatively assessed with a reliability index, R_{AB} (Winkelmann et al., 1991; Baker et al., 1991). A plot of R_{AB} for Cabb-B vs CM1841 shows that the two density maps agree quite well out to a resolution of $\sim 3 \text{ nm}$ (Fig. 6). Slight disagreement between Cabb-B and CM1841 at low resolution ($\sim 0.1 \text{ nm}^{-1}$) is attributed to the presence of additional density at low radii in layer III of Cabb-B which makes this layer slightly thicker than that in CM1841. The sharp rise in R_{AB} at spatial frequencies $> 0.34 \text{ nm}^{-1}$ is attributed to noise in the image data which dominates especially where the CTF drops to a minimum (Fig. 3). Thus, a realistic estimate of the reliable resolution of the reconstructions is $\sim 3 \text{ nm}$.

Visual inspection of the Cabb-B and CM1841 density maps confirms their similarity. Therefore, only illustrations of the Cabb-B structure are presented hereafter, and further discussions of CaMV structure are assumed to be equivalent for both Cabb-B and CM1841.

420 Subunit, pentamer-hexamer capsid

Projected images of the density, contained just within the outermost CaMV layer ($r > 21.2 \text{ nm}$) and viewed along radial directions parallel to the axes of the pentavalent (Figs. 7A and 7B) and hexavalent (Figs. 7C and 7D) capsomers, clearly reveal pentameric and hexameric capsomer morphologies. This suggests that CaMV is composed of 420 “subunits,” 60 from the 12 pentamers and 360 from the 60 hexamers. The pentavalent pentamer, with strict fivefold symmetry imposed by the icosahedral averaging procedure, has a pentagonal outer profile of maximum dimension $\sim 8.3 \text{ nm}$ with a central region of weak density of radius $\sim 1.4 \text{ nm}$. Each pentamer subunit has an approximately elliptical shape (3.1 by 2.7 nm) and

²All solvent at radii $> 22.9 \text{ nm}$ except for that in the cavities centered about the capsomer axes (Fig. 4).

contacts two neighboring, equivalent pentamer subunits (with a center-to-center inter-subunit spacing of 3 nm) and a third sub-unit from an adjacent hexamer. Although the hexavalent capsomers are unquestionably hexameric, the six subunits are arranged with quasi-twofold, not quasi-sixfold symmetry as might be expected for a $T = 7$ structure organized with quasi-equivalent symmetry as originally proposed by Caspar and Klug (1962). The hexamer seems to be subdivided into two similar halves, each consisting of three subunits, two of which form a closely associated pair (Fig. 7D, “dumbbell” symbols). An identical “distorted” hexameric arrangement of subunits is also seen in CaMV CM1841 (data not shown). This provides compelling evidence that the distorted subunit arrangement is a genuine feature of the CaMV structure and not an artifact of the imaging or reconstruction processes. The largest dimension of the hexamer is ~ 10.3 nm, and the subunits are ~ 3 nm in diameter. The center-to-center spacing between hexamer subunits ranges between 3.0 and 3.8 nm. The number and distorted arrangement of these subunits gives the hexamer a larger, less-dense center ($r = 2$ nm) than that in the pentamer. Five of the six hexamer subunits appear to make strong contacts with individual subunits from five neighboring capsomers. The remaining hexamer subunit, closest to the strict icosahedral twofold axis, appears to make weaker contact (Fig. 7D, arrowhead) with the twofold related subunit in the sixth neighboring capsomer. At the level of the outermost layer of the CaMV virion, all 420 subunits thus appear to participate in three inter-subunit interactions, two with subunits in the same capsomer and the third with a subunit of an adjacent capsomer.

Multilayer virion

The multilayer CaMV structure can be systematically examined in solid-surface views of the reconstruction, truncated at progressively lower radii (Figs. 8A–8K) and in projections of the reconstructed density at specific radii (Figs. 8L–8R). These displays, along with a surface-shaded view of the virion cross-sectioned along a plane that includes the axes of both capsomers (Fig. 8S), suggest the presence of more extensive contact between layers II and III compared to layers I and II (cf. Figs. 8G and 8I). A large volume of contiguous, solvent-accessible space separates layers I and II, and large cone-shaped cavities (3.3 and 4.4 nm high; 6.6 and 8.8 nm dia. at the bases) exist beneath both types of capsomers (Fig. 8S). An intricate network of cavities and channels characterize the open CaMV structure.

At the contour level chosen to depict solid density in Fig. 8, (i) the cavity beneath the hexamer is accessible to the virion surface through an axial opening ~ 1 nm in diameter (Figs. 8A, 8E, and 8S), (ii) a smaller cavity beneath the pentamer is closed off from the outside along the fivefold axis (Figs. 8A, 8E, and 8S), (iii) the thicknesses of both capsomers are relatively uniform (~ 2.2 nm, Fig. 8S), (iv) the pentamer extends to a maximum radius slightly larger (26.9 nm vs 26.4 nm) than that of the hexamer (Fig. 8S), (v) a series of tangential channels interconnect the cavities between layers I and II (Fig. 8S), (vi) solvent from the outside is mainly accessible to layer II via the axial channels of the 60 hexamers and the 140 holes at the 20 strict and 120 quasi-threefold positions (Figs. 8A, 8E, 8F, and 8S), (vii) layer III appears to be the most contiguous layer and seems mainly accessible to solvent through small openings in layer II along or near the 72 capsomer axes (Figs. 8F–8I and 8M–8P), (viii) the virion core appears to be inaccessible to solvent (Figs. 8I and 8J), and (ix) cilia-like density features that radially project ~ 3 nm from the inner wall of the virion

into the large, central cavity (Figs. 8D, 8K, 8R, and 8S) account for the shoulder of density seen in the radial density plot (Fig. 5).

Layer I contains the highest density features in the icosahedrally symmetrized map (Figs. 8L–8N). Thus, compared to the density of layers II and III, the organization of density in layer I is the easiest to interpret as it is the density in the virion most consistent with an icosahedral arrangement. The lower average density of layers II and III is likely the result of smearing caused by averaging regions which do not conform to the icosahedral symmetry of the outer layer. Density features within layers II and III appear more complex, have less well-defined connectivity, and therefore are more difficult to interpret with confidence (Figs. 8O–8R). The densest regions of layers II and III appear as nearly space-filled features in the surface-rendered views (Figs. 8H and 8J), although this gives a somewhat misleading impression since the corresponding density distributions at the respective radii (Figs. 8O and 8Q) reveal nonuniform distributions. With the possible exception of density close to the fivefold axes, there is no clearly defined connectivity between the density features attributed to the icosahedrally symmetric capsomers at high radii (layer I) and the density features at lower radii (layers II and III).

Discussion

CaMV is the first $T = 7$ isometric plant virus to be studied by cryo-electron microscopy and image reconstruction methods. Cabb-B is aphid transmissible and causes severe disease symptoms, whereas CM1841 is a mild strain which can only be transmitted by mechanical inoculation (Lung and Pirone, 1973). The remarkable consistency between the reconstructions obtained from these two strains of CaMV of distinct phenotype strongly suggests that all strains of CaMV have the same basic structure.

$T = 7$, 420-subunit outer capsid model: Comparison with papovaviruses

Our analyses of unstained, frozen-hydrated samples of two isolates of CaMV clearly establish a 420-subunit model for the structure of the outer virion layer. The protein and nucleic acid components are organized in three concentric layers surrounding a large, empty core. CaMV is the first example of a simple, spherical virus with $T = 7$ icosahedral lattice symmetry that conforms to the rules of stoichiometry for isometric viruses as originally formulated by Caspar and Klug (1962). That is, the 420 subunits that form the outer layer are organized as 72 capsomeric aggregates, in which the 12 pentavalent capsomers are pentamers and the 60 hexavalent capsomers are hexamers. This contrasts with the all-pentamer, 360-subunit capsid structure observed for four members of the $T = 7$ papovavirus family (Rayment et al., 1982; Baker et al., 1988, 1989, 1991).

Despite early indications of a close relationship between the caulimoviruses and the polyoma-type³ viruses (Tezuka and Taniguchi, 1972; Hull and Shepherd, 1976), these viruses are now clearly distinguished by several, well-established properties. CaMV and polyoma are similar-sized, isometric viruses (53.8 nm vs 49.5 nm dia.), each with $T = 7$

³The term “polyoma” is used here to collectively refer to all viruses within the polyomavirinae subfamily (e.g., polyoma, SV40, BKV, JCV, etc.).

icosahedral surface lattice symmetry and having a single, circular (closed) dsDNA genome and a major capsid protein of similar mass (~40 kDa). However, the CaMV genome is larger (~8000 vs ~5000 bp), is organized differently, codes for a distinct set of gene products, and is not associated with host-encoded histones as is the polyoma DNA (e.g., Griffith, 1975). Two prominent structural differences contrast CaMV and polyoma: (i) the stoichiometries and quaternary organizations of the respective major capsid proteins are distinctly different (i.e., 72 pentameric capsomers for polyoma), and (ii) the “core” of CaMV is empty, whereas polyoma contains a minichromosome “core.” Interestingly, both viruses display marked departures from classic quasi-equivalent packing arrangements of the capsid subunits (Caspar and Klug, 1962) although this must be manifest in distinctly different ways since the respective hexavalent capsomers have different oligomeric states. The dsDNA is packaged at a high radius in CaMV and appears to be in close contact with virion-coded proteins, whereas polyoma dsDNA is complexed with cellular histones in a central nucleohistone core of diameter 33 nm (Baker et al., 1988).

Correlation with multilayer neutron scattering model

The multilayer structure observed for the Cabb-B and CM1841 strains of CaMV is consistent with a similar, multilayer model (Fig. 9) proposed on the basis of neutron solution scattering experiments on strain D/H (Kruse et al., 1987). The Kruse et al. (1987) model consists of four concentric layers, each with different amounts of protein and DNA: (i) an outermost layer (radii 21.5–25.0 nm) composed only of protein (60% of total virion protein), (ii) a second layer (radii 18.5–21.5 nm) composed of 42% of the total DNA and 26% of the total protein, (iii) a third layer (radii 15.0–18.5 nm) mainly consisting of DNA (52%; 3% protein), and (iv) an innermost layer (radii 12.0–15.0 nm) containing the smallest amount of protein (11%) and DNA (6%). In this model, the large volume fraction of water in each of these layers (57, 59, 78, and 74%, respectively) indicates that the packing density of components in CaMV virions is not as high, for example, as that found in most smaller plant viruses including the swollen forms of small isometric RNA viruses (Kruse et al, 1982). This unusually low density, which has been viewed as somewhat surprising given the high stability of CaMV virions in extreme environmental conditions (e.g., Al Ani et al., 1979a), is completely consistent with the open structure seen in the two image reconstructions presented here (Fig. 4). The low packing density in CaMV is also consistent with the interpretation of sedimentation and diffusion coefficient measurements which indicated that CaMV has an average, effective hydrated diameter of 57 nm (Hull et al., 1976).

The primary difference between the image reconstruction and neutron scattering results (Fig. 9) concerns a delineation of layer III of the reconstruction as two separate layers in the neutron model. Inspection of the reconstructions leads us to conclude that there are three, clearly-defined layers, with the third layer consisting of a contiguous region at high radius (14.5–17.6 nm; Fig. 5) from which 80 small protrusions of density radiate toward the solvent-filled virion center (11.4–14.5 nm; Figs. 8D and 8S). The continuity of density in this region (11.4–17.6 nm) suggests that all such density be attributed to a single “layer” (III). From the combined neutron and microscopy studies (Fig. 9), it thus appears that CaMV consists of an outer, primarily proteinaceous layer (I) that displays icosahedral symmetry, and two prominent inner layers (II, III) that have no well-defined symmetrical arrangements

of the DNA and protein. Layers II and III both contain protein and DNA, but these components appear to be partially segregated in layer III with the DNA mainly confined to higher radii (Fig. 9).

Organization of protein and DNA

There is no reliable way to accurately discriminate the protein and DNA components of CaMV in reconstructions computed from images recorded at a single level of defocus or from images of samples that were all embedded in vitrified solutions with the same solvent density (Lepault et al., 1983; Lepault, 1985). However, a self-consistent model for the structure of gpIV can be proposed based on (i) knowledge that gpIV is present as 37 kDa and 42 kDa polypeptides in approximately a six to one ratio (Al Ani et al., 1979b; Kruse et al., 1987; Martínez-Izquierdo and Hohn, 1987; unpublished data), (ii) examination of structural features in the reconstructions, (iii) calculations of solvent-excluded volumes from our results and the neutron scattering model of Kruse et al. (1987), and (iv) consideration of the basic tenets of the replication-assembly model of Hull et al. (1987).

The total virion volume is $\sim 64,000 \text{ nm}^3$. Sixty-eight percent of this volume ($43,300 \text{ nm}^3$) is attributed to solvent inside the virion (one-third of which is accounted for by the large, central cavity), leaving $\sim 20,700 \text{ nm}^3$ for packaging the total virion protein and DNA. If the virion is composed solely of 420 copies of 37 kDa gpIV and one dsDNA molecule, then each gpIV molecule must extend the entire 15.5-nm virion thickness (radii 11.4–26.9 nm) and may be subdivided such that 21, 9, and 7 kDa portions of the molecule are respectively distributed among layers I–III. The sizes of these portions of gpIV are entirely consistent with neutron scattering data (Kruse et al., 1987) and analysis of amino-acid sequence data (Devereux et al., 1984; Hull et al., 1987; unpublished results). This strongly suggests that gpIV has a multi-domain tertiary structure.

Evidence suggests that the N-terminal portion of the proposed gpIV molecule is exposed to the external surface of the virion (Hull et al., 1987; Ménissier-de Murcia et al., 1986). The 21-kDa N-terminal portion of gpIV could form one “domain” that is symmetrically arranged in the prominent capsomer aggregates in layer I. We predict this “domain” adopts the common, eight-stranded, β -barrel structure, which to date has been found as the basic structural motif in the capsid subunits of most isometric viruses, including all isometric plant viruses studied by high resolution crystallographic techniques (e.g., Rossmann and Johnson, 1989). This common structural motif has a minimum size of 15–16 kDa, but it typically resides within sub-unit domains of 20–25 kDa.

The second ($\sim 9 \text{ kDa}$) “domain” of gpIV is postulated to reside within layer II where it would bind the DNA. CaMV coat protein possesses an unusually high lysine content (18% on a molar basis of the amino acid content of total virion protein; Brunt et al., 1975) that is mainly localized in an $\sim 8\text{-kDa}$ region of the sequence adjacent to the 21-kDa N-terminal half of the molecule. A “Cys” motif lies immediately to the C-terminal side of this basic stretch of polypeptide (Hull et al., 1987). The combined Lys-rich and Cys-motif regions span $\sim 9 \text{ kDa}$ of the sequence and both regions demonstrate strong nucleic acid binding potential (Franck et al., 1980; Berg, 1986). Strong interactions between gpIV and the DNA are consistent with the observation that viral DNA partially unfolds and extrudes from

virions at pH 11.25 but reversibly reassembles upon lowering of the pH (Al Ani et al., 1979a). The chemical stability of CaMV may thus be accounted in part by nonspecific electrostatic interactions between negatively charged portions of the DNA and positively charged (basic) portions of gpIV. Additional stability may arise from van der Waals interactions between the nucleotide bases and the folded gpIV polypeptide.

The remaining 7 kDa at the C-terminus of gpIV would be distributed in layer III, probably with most of it exposed to the central cavity at the inner virion wall (Fig. 9). In this model for gpIV, the N- and C-terminal domains would essentially form a protein “sandwich” for the DNA contained in layer II and at the higher radius portion of layer III. In contrast with this gpIV model, the C-terminal portions of capsid proteins in isometric viruses are exposed at the viral surface (Rossmann and Johnson, 1989; one notable exception to this is the 44-kDa capsid protein of black beetle virus as reported by Hosur et al. (1987)). However, our gpIV model is consistent with this general rule since the C-terminal portion is, in a strict sense, at a surface because it is “exposed” to the large, solvent-filled cavity.

Structural flexibility and implications for assembly and infection

Little is known about the details of CaMV assembly, although the process is known to occur in the viroplasm (inclusion bodies) of infected plant cells where the DNA is also replicated (Hull et al., 1987; Rodriguez et al., 1988). A possible close coupling of assembly and replication may in part account for the characteristic open, flexible structure of mature virions. If these processes are spatially and temporally closely coupled as suggested, then some fraction of the 76-kDa reverse transcriptase, gpV, may remain associated with maturing particles, subsequently get trapped inside the “empty” virion core, and generate cavities or holes inside the virion after dissociating from the assembly complex. Indeed, gpV has been shown to be associated with virus particles in purified preparations of CaMV (Ménissier et al., 1984; Gordon et al., 1988). A model for assembly proposed by Hull et al. (1987) indicates that within the viroplasm there is a close interaction between the 61-kDa inclusion body protein, gpVI, and the N-terminal, acid-rich and phosphorylated portion (11 kDa) of the 58-kDa major capsid precursor protein, gpIV. Proteolysis later cleaves this 11-kDa region and also a 4-kDa C-terminal region from gpIV to produce the primary 42-kDa capsid protein (Franck et al., 1980). These gpIV fragments and gpVI are not detected in mature virions. Thus, gpVI may serve a scaffold role to help nucleate coat protein assembly. The large holes that are observed in the surface of mature virions (Figs. 4 and 8) might therefore be the vestiges of gpVI and the other protein fragments after they have left the assembly complex. Holes and cavities generated by the loss of such components may either serve to increase structural flexibility or to provide pathways to ultimately facilitate the release of the dsDNA genome upon infection of new cell tissue. In addition, these cavities may provide access to the dsDNA by ions, small molecules or macromolecules (e.g., gpIII, Giband et al., 1986; Gordon et al., 1988; Mesnard et al., 1990).

The atypical, solvent-filled CaMV structure may explain why it easily distorts and why so many difficulties were encountered during the analysis of image data and in computing reliable reconstructions. Only a small fraction of particle images exhibited minimal departure from icosahedral symmetry and were successfully included in the data analysis

used to compute the three-dimensional reconstructions (Fig. 4). Structural flexibility in CaMV apparently arises due to the rather low packing density of the protein–DNA components. Heterogeneity, which can arise from the presence of minor proteins or from variable amounts of proteins that remain associated with mature particles, may disrupt an otherwise stable, symmetrical structure. For example, in addition to molecules of gpV that may get trapped inside the center of virions during assembly, an 11-kDa protein, which arises from proteolysis of the C-terminal region of the 15-kDa product of ORF III, is thought to be a minor structural component on the surface of virions (Giband et al., 1986; Gordon et al., 1988; Mesnard et al., 1990).

Conditions for forming large, single crystals of CaMV CM1841 for X-ray crystallographic studies were recently reported (Gong et al., 1990). These crystals diffracted only to 2.7 nm resolution. This limited resolution was ascribed to variability in proteolysis of the coat protein *in vivo* (Burger and Du Plessis, 1983) and during isolation and purification (Gong et al., 1990). Flexibility and heterogeneity in CaMV could explain why high resolution structural details have yet to be determined.

Acknowledgments

We thank Z. X. Gong, R. Hull, J. E. Johnson, M. G. Rossmann, and R. J. Shepherd for stimulating discussions, and C. E. Bracker, R. Lister, and A. Prongay for critical review of the manuscript. We gratefully acknowledge J. Bibler, Z. X. Gong, R. Richins, R. J. Shepherd, S. Y. Song, and H. Wu for CaMV samples; W. Murakami for polyoma samples; D. Furlong for reovirus samples; N. R. Dilley, K. A. Dryden, and W. D. Grochulski for programs; D. M. Belnap for magnification calibration calculations; and G. J. Wang and W. Xu for assistance with electron microscopy. This work was initially funded by National Institutes of Health Grant GM33050 (TSB), and by National Science Foundation Grant DMB-8602753 (M. G. Rossmann), and has since been funded by National Science Foundation Grant DMB-8905062 (TSB), and a grant from the Lucille P. Markey Charitable Trust for the development of structural studies at Purdue.

References

- Al Ani R, Pfeiffer P, Lebourier G, Hirth L. The structure of cauliflower mosaic virus. I pH-induced structural changes *Virology*. 1979a; 93:175–187.
- Al Ani R, Pfeiffer P, Lebourier G. The structure of cauliflower mosaic virus. II. Identity and location of the viral polypeptides. *Virology*. 1979b; 93:188–197. [PubMed: 433152]
- Baker TS, Drak J, Bina M. Reconstruction of the three-dimensional structure of simian virus 40 and visualization of the chromatin core. *Proc Natl Acad Sci USA*. 1988; 85:422–426. [PubMed: 2829185]
- Baker TS, Drak J, Bina M. The capsid of small papova viruses contains 72 pentameric capsomeres: Direct evidence from cryo-electron-microscopy of simian virus 40. *Biophys J*. 1989; 55:243–253. [PubMed: 2540847]
- Baker TS, Newcomb WW, Booy FP, Brown JC, Steven AC. Three-dimensional structures of maturable and abortive capsids of equine herpesvirus 1 from cryoelectron microscopy. *J Virol*. 1990; 64:563–573. [PubMed: 2153224]
- Baker TS, Newcomb WW, Olson NH, Cowsert LM, Olson C, Brown JC. Structure of bovine and human papillomaviruses: Analysis by cryoelectron microscopy and three-dimensional image reconstruction. *Biophys J*. 1991; 60:1445–1456. [PubMed: 1663794]
- Bălazs E, Guilley H, Jonard G, Richards K. Nucleotide sequence of DNA from an altered-virulence isolate D/H of the cauliflower mosaic virus. *Gene*. 1982; 19:239–249. [PubMed: 7152260]
- Berg JM. Protein metal-binding domains in nucleic acid binding protein. *Science*. 1986; 232:485–487. [PubMed: 2421409]

- Brisson N, Paszkowski J, Penswick JR, Gronenborn I, Potrykus I, Hohn T. Expression of a bacterial gene in plants by using a viral vector. *Nature*. 1984; 310:511–514.
- Brunt AA, Barton RJ, Tremaine JH, Stace-Smith R. The composition of cauliflower mosaic virus protein. *J Gen Virol*. 1975; 27:101–106.
- Burger JG, Du Plessis D. Detection of partially proteolysed cauliflower mosaic virus. *J Virol Methods*. 1983; 7:11–19. [PubMed: 6352722]
- Caspar DLD, Klug A. Physical principles in the construction of regular viruses. *Cold Spring Harb Symp Quant Biol*. 1962; 27:1–24. [PubMed: 14019094]
- Cheng RH, Olson NH, Baker TS. Cryo-electron microscopy of cauliflower mosaic virus. *Proc Elec Microsc Soc Am (San Antonio)*. 1989; 47:824–825.
- Chauvin C, Jacrot B, Lebeurier G, Hirth L. The structure of cauliflower mosaic virus: a neutron diffraction study. *Virology*. 1979; 96:640–641. [PubMed: 18631597]
- Crowther RA, Amos LA, Finch JT, De Rosier DJ, Klug A. Three dimensional reconstructions of spherical viruses by Fourier synthesis from electron micrographs. *Nature*. 1970; 226:421–425. [PubMed: 4314822]
- Crowther RA. Procedures for three-dimensional reconstruction of spherical viruses by Fourier synthesis from electron micrographs. *Phil Trans Roy Soc Lond B*. 1971; 261:221–230. [PubMed: 4399207]
- Day MG, Venables DG. Purification of cauliflower mosaic virus. *Virology*. 1960; 11:502–505. [PubMed: 13814596]
- Devereux J, Haebeli P, Smithies O. A comprehensive set of sequence analysis programs for the VAX. *Nucleic Acids Res*. 1984; 12:387–395. [PubMed: 6546423]
- De Zoeten GA, Penswick JR, Horisberger MA, Ahl P, Schultze M, Hohn T. The expression, localization, and effect of a human interferon in plants. *Virology*. 1989; 172:213–222. [PubMed: 2773316]
- Dubochet J, Adrian M, Chang JJ, Homo JC, Lepault J, McDowell A, Schultz P. Cryo-electron microscopy of vitrified specimens. *Q Rev Biophys*. 1988; 21:129–228. [PubMed: 3043536]
- Du Plessis DH, Smith P. Glycosylation of the cauliflower mosaic virus capsid polypeptide. *Virology*. 1981; 109:403–408. [PubMed: 18635040]
- Erickson HP, Klug A. Measurement and compensation of defocusing and aberrations by Fourier processing of electron micrographs. *Phil Trans Roy Soc Lond B*. 1971; 261:105–118.
- Franck A, Guillely H, Jonard G, Richards K, Hirth L. Nucleotide sequence of cauliflower mosaic virus DNA. *Cell*. 1980; 21:285–294. [PubMed: 7407912]
- Fujisawa I, Rubio-Huertos M, Matsui C, Yamaguchi A. Intracellular appearance of cauliflower mosaic virus particles. *Phytopathology*. 1967; 57:1130–1132.
- Fuller SD. The $T = 4$ envelope of Sindbis virus is organized by interactions with a complementary $T = 3$ capsid. *Cell*. 1987; 48:923–934. [PubMed: 3829124]
- Gardner RC, Howarth AJ, Hahn P, Brown-Luedi M, Shepherd RJ, Messing J. The complete nucleotide sequence of an infectious clone of cauliflower mosaic virus by M13mp7 shotgun sequencing. *Nucleic Acids Res*. 1981; 9:2871–2888. [PubMed: 6269062]
- Giband M, Mesnard JM, Lebeurier G. The gene III product (P15) of cauliflower mosaic virus is a DNA-binding protein while an immunologically related P11 polypeptide is associated with virions. *EMBO J*. 1986; 5:2433–2438. [PubMed: 16453711]
- Gong ZX, Wu H, Cheng RH, Hull R, Rossmann MG. Crystallization of cauliflower mosaic virus. *Virology*. 1990; 179:941–945. [PubMed: 2238483]
- Gordon K, Pfeiffer P, Fütterer J, Hohn T. *In vitro* expression of cauliflower mosaic virus genes. *EMBO J*. 1988; 7:309–317. [PubMed: 16453827]
- Griffith JD. Chromatin structure: Deduced from a mini-chromosome. *Science*. 1975; 187:1202–1203. [PubMed: 17754289]
- Hahn P, Shephard RJ. Phosphorylated proteins in cauliflower mosaic virus. *Virology*. 1980; 107:295–297. [PubMed: 18631810]
- Hahn P, Shephard RJ. Evidence for a 58-kilodalton polypeptide as precursor of the coat protein of cauliflower mosaic virus. *Virology*. 1982; 116:480–488. [PubMed: 18635117]

- Hills GL, Campbell RN. Morphology of broccoli necrotic yellow virus. *J Ultrastruc Res.* 1968; 24:134–144.
- Hohn T, Hohn B, Pfeiffer P. Reverse transcription in a plant virus. *Trends Biochem Sci.* 1985; 10:205–209.
- Hosur MV, Schmidt T, Tucker RC, Johnson JE, Gallagher TM, Selling BH, Rueckert RR. Structure of an insect virus at 3.0 Å resolution. *Proteins: Struct Func Genet.* 1987; 2:167–176.
- Hull R, Shephard RJ, Harvey JD. Cauliflower mosaic virus: an improved purification procedure and some properties of the virus particles. *J Gen Virol.* 1976; 31:93–100.
- Hull R, Shephard RJ. The coat proteins of cauliflower mosaic virus. *Virology.* 1976; 70:217–220. [PubMed: 1258379]
- Hull R, Covey SN, Maule AJ. Structure and replication of caulimovirus genomes. *J Cell Sci (Suppl).* 1987; 7:213–229. [PubMed: 3332654]
- Itoh T, Matsui C, Hirth T. Conformational changes in cauliflower mosaic virus. *Virology.* 1969; 39:367–372. [PubMed: 5358075]
- Kruse J, Timmins PA, Witz J. A neutron scattering study of the structure of compact and swollen forms of southern bean mosaic virus. *Virology.* 1982; 119:42–50. [PubMed: 18635139]
- Kruse J, Timmins PA, Witz J. The spherically averaged structure of a DNA isometric plant virus: Cauliflower mosaic virus. *Virology.* 1987; 159:166–168. [PubMed: 18644567]
- Lefebvre DD, Miki BL, Laliberté JF. Mammalian metallothionein functions in plants. *Bio/Tech.* 1987; 5:1053–1056.
- Lepault J, Booy FP, Dubochet J. Electron microscopy of frozen biological suspensions. *J Microsc.* 1983; 129:89–102. [PubMed: 6186816]
- Lepault J. Cryo-electron microscopy of helical particles. *J Microsc.* 1985; 140:73–80. [PubMed: 4093967]
- Lung MCY, Pirone TP. Studies on the reason for differential transmissibility of cauliflower mosaic virus isolates by aphids. *Phytopathology.* 1973; 63:910–914.
- Mandahar, CL. Plant DNA viruses. In: Mandahar, CL., editor. *Plant Viruses I Structure and Replication.* CRC Press; FL: 1989. p. 235-258.
- Martínez-Izquierdo J, Hohn T. Cauliflower mosaic virus coat protein is phosphorylated *in vitro* by a virion-associated protein kinase. *Proc Natl Acad Sci USA.* 1987; 84:1824–1828. [PubMed: 16593818]
- Maule AJ, Harker CL, Wilson IG. The pattern of accumulation of cauliflower mosaic virus-specific products in infected turnips. *Virology.* 1989; 169:436–446. [PubMed: 2705305]
- Ménissier J, Laquel P, Lebeurier G, Hirth L. A DNA polymerase activity is associated with cauliflower mosaic virus. *Nucleic Acids Res.* 1984; 12:8769–8777. [PubMed: 6514573]
- Ménissier-de Murcia J, Geldreich A, Lebeurier G. Evidence for a protein kinase activity associated with purified particles of cauliflower mosaic virus. *J Gen Virol.* 1986; 67:1885–1891.
- Mesnard JM, Kirchherr D, Wurch T, Lebeurier G. The cauliflower mosaic virus gene III product is a non-sequence-specific DNA binding protein. *Virology.* 1990; 174:622–624. [PubMed: 2305555]
- Olson NH, Baker TS. Magnification calibration and the determination of spherical virus diameters using cryo-microscopy. *Ultramicroscopy.* 1989; 30:281–298. [PubMed: 2800042]
- Pirone TP, Pound GS, Shepherd RJ. Properties and serology of purified cauliflower mosaic virus. *Phytopathology.* 1961; 51:541–547.
- Rayment I, Baker TS, Caspar DLD, Murakami WT. Polyoma virus capsid structure at 22.5 Å resolution. *Nature.* 1982; 295:110–115. [PubMed: 6276752]
- Rodríguez D, López-Abella D, Díaz-Ruiz JR. An electron microscopic study of cauliflower mosaic virus-induced viroplasm: unusual structures within the viroplasm matrix with possible functional significance in the viral replication cycle. *J Ultrastructure and Mol Structure Res.* 1988; 100:118–125.
- Rossmann MG, Johnson JE. Icosahedral RNA virus structure. *Annu Rev Biochem.* 1989; 58:533–573. [PubMed: 2673017]
- Rubio-Huertos M, Matsui C, Yamaguchi A, Kamei T. Electron microscopy of x-body formation in cells of cabbage infected with *Brassica* virus 3. *Phytopathology.* 1968; 58:548–549.

- Sanfaçon H, Hohn T. Proximity to the promoter inhibits recognition of cauliflower mosaic virus polyadenylation signal. *Nature*. 1990; 346:81–84. [PubMed: 2366867]
- Shepherd RJ, Bruening GE, Wakeman RJ. Double-stranded DNA from cauliflower mosaic virus. *Virology*. 1970; 41:339–347. [PubMed: 4316313]
- Steven AC, Hainfeld JF, Trus BL, Steinert PM, Wall JS. Radial distributions of density within macromolecular complexes determined from dark-field electron micrographs. *Proc Natl Acad Sci USA*. 1984; 81:6363–6367. [PubMed: 6593706]
- Stewart M, Vigers G. Electron microscopy of frozen-hydrated biological material. *Nature*. 1986; 319:631–636. [PubMed: 3951536]
- Stewart, M. Electron microscopy of biological macromolecules: Frozen-hydrated methods and computer image processing. In: Duke, PJ.; Michertte, AG., editors. *Modern Microscopies: Techniques and Applications*. Plenum Press; New York: 1990. p. 9-39.
- Tezuka N, Taniguchi T. Stepwise degradation of cauliflower mosaic virus by pronase. *Virology*. 1972; 47:142–146. [PubMed: 5058330]
- Toyoshima C, Unwin N. Contrast transfer for frozen-hydrated specimens: Determination from pairs of defocused images. *Ultramicrosc*. 1988; 25:279–292.
- Vogel RH, Provencher SW, von Bonsdorff CH, Adrian M, Dubochet J. Envelope structure of Semliki Forest virus reconstructed from cryo-electron micrographs. *Nature*. 1986; 320:533–535. [PubMed: 3960136]
- Winkelman DA, Baker TS, Rayment I. Three-dimensional structure of myosin subfragment-1 from electron microscopy of sectioned crystals. *J Cell Biol*. 1991; 114:701–713. [PubMed: 1869586]
- Yeager M, Dryden KA, Olson NH, Greenberg HB, Baker TS. Three-dimensional structure of Rhesus rotavirus by cryoelectron microscopy and image reconstruction. *J Cell Biol*. 1990; 110:2133–2144. [PubMed: 2161857]

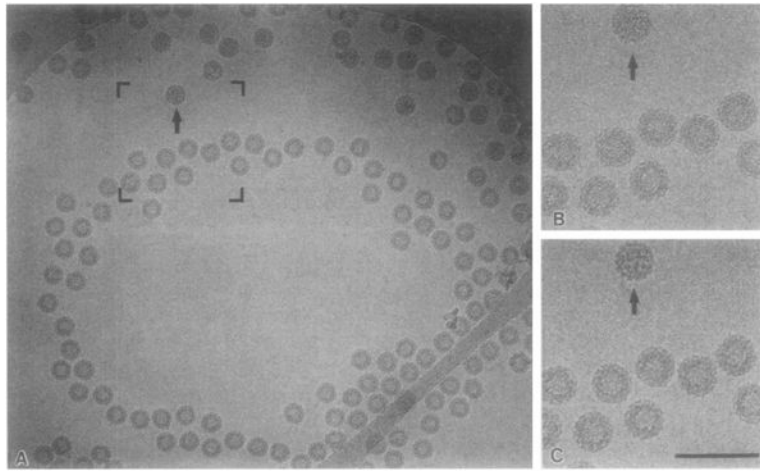


Fig. 1.

(A) Micrograph of a vitrified CaMV sample, suspended over holes in a carbon support film, containing polyoma virus (arrow) as an internal calibration standard. (B) Magnified view of the same area as (A) shown in brackets, but recorded prior to (A) at $\sim 1.2 \mu\text{m}$ underfocus and with an electron dose of $\sim 1200 \text{ e}^-/\text{nm}^2$. (C) Magnified view of (A) recorded at $\sim 2.4 \mu\text{m}$ underfocus and with an accumulated specimen dose of $\sim 2400 \text{ e}^-/\text{nm}^2$. The higher phase contrast of (C) compared to (B) helped facilitate initial refinement of particle orientation and alignment parameters. The bar in (C) represents 200 nm in (A) and 100 nm in (B) and (C).

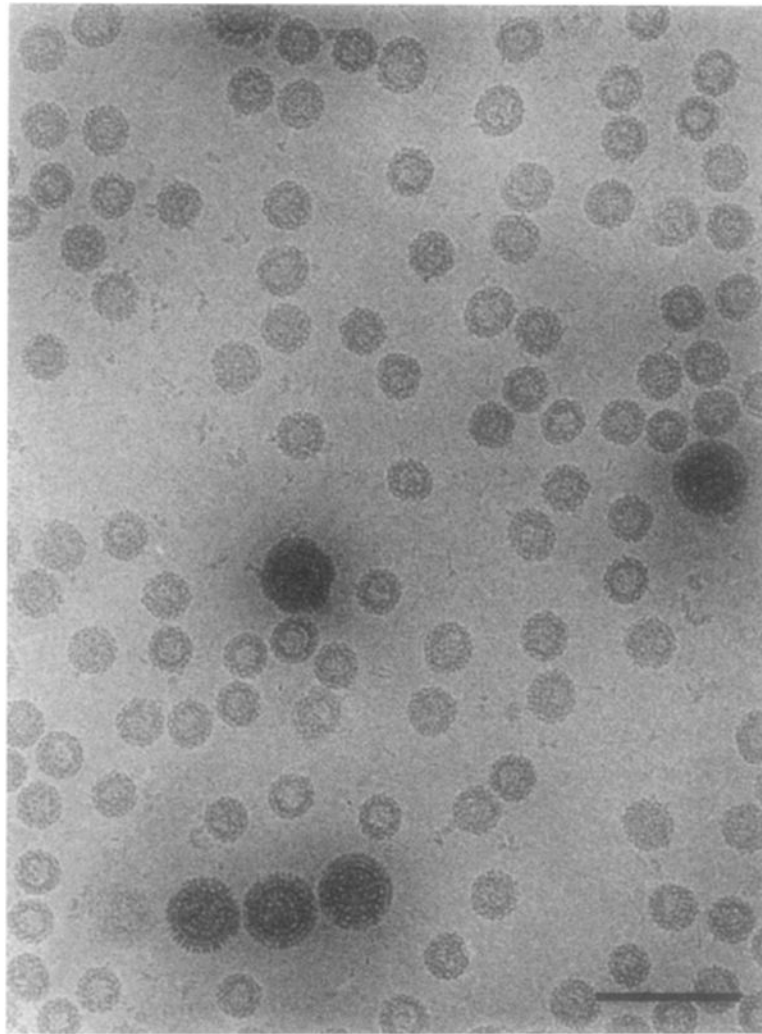


Fig. 2. Micrograph of a vitrified solution containing CaMV and Type-1 reovirus virions. The diameters of CaMV in this (typical) sample vary by as much as 30%. Those CaMV particles that exhibit the most uniformly round profiles, and therefore are believed to have the best preserved icosahedral symmetry, usually occur in the thicker regions of the vitrified sample near the larger (~80 nm dia.) reovirus particles. Bar \simeq 200 nm.

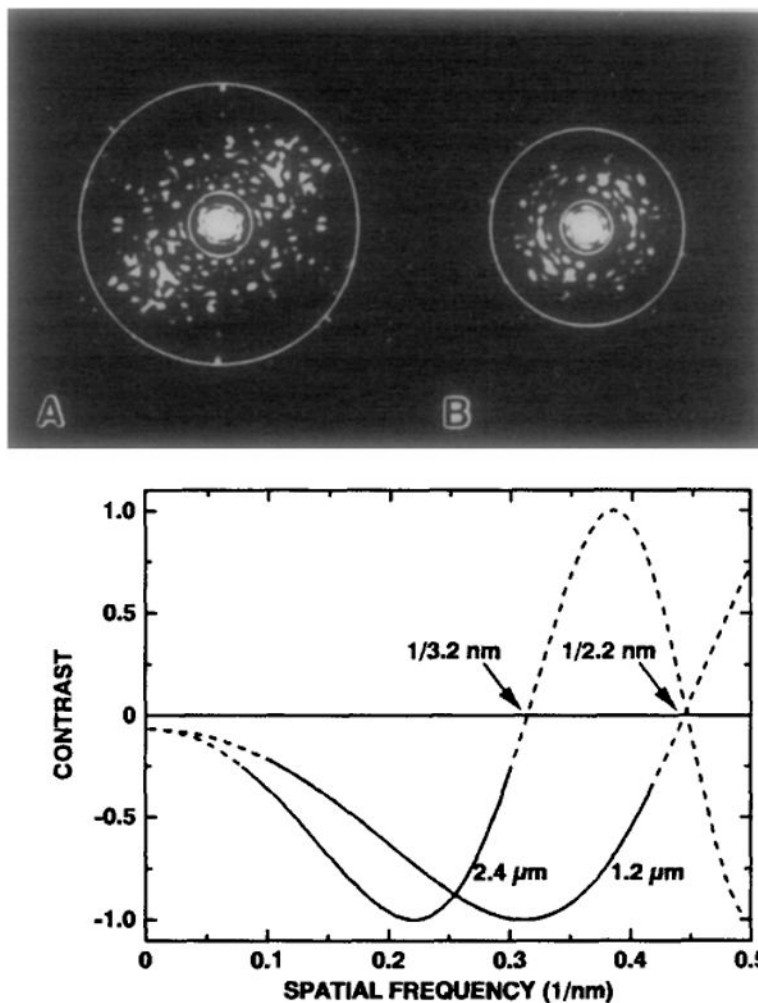


Fig. 3. (A,B) Fourier transforms computed from a focal pair of images of a single CaMV virion recorded at $\sim 1.2 \mu\text{m}$ (A) and $\sim 2.4 \mu\text{m}$ underfocus (B). White circles mark annular regions from each transform (between $(1/10.7) \text{ nm}^{-1}$ and $(1/2.4) \text{ nm}^{-1}$ in (A) and between $(1/12.8) \text{ nm}^{-1}$ and $(1/3.4) \text{ nm}^{-1}$ in (B)) used in the particle orientation refinement procedures. (C) Theoretical plots of the microscope contrast transfer functions (CTFs) corresponding to the defocus settings used in the images from which (A) and (B) were computed. The CTFs, $A(\theta)\sin\chi(\theta) + B(\theta)\cos\chi(\theta)$, are plotted as a function of spatial frequency, θ/λ , in nm^{-1} , for $\lambda = 0.0042 \text{ nm}$ (the wavelength of 80 kV electrons), $C_s = 2 \text{ mm}$ (objective lens spherical aberration coefficient), and assuming that amplitude contrast remains constant (7%) over the range of spatial frequencies depicted (see Toyoshima and Unwin (1988) for a complete description of how CTFs are computed). The solid portions of the CTF curves correspond to the regions of the Fourier transform bounded by the circles in (A) and (B). The first minima (zeroes) in the respective transforms occur at $(1/2.2) \text{ nm}^{-1}$ and $(1/3.2) \text{ nm}^{-1}$ (just outside the large white circles).

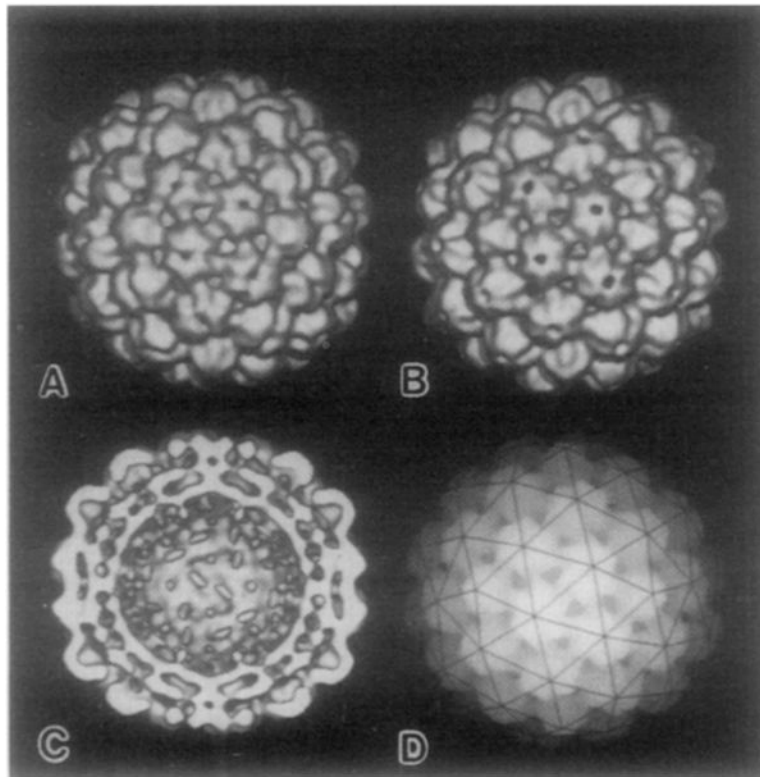


Fig. 4. (A, B) Surface-shaded representations of the CaMV Cabb-B (A) and CM1841 (B) reconstructions, computed from 21 and 40 independent particle images, respectively, and viewed along an icosahedral twofold axis of symmetry. (C) Cutaway view of the back half of (A), reveals a multilayered internal structure and a large, central cavity. The equivalent view of CM1841 (not shown) is essentially identical to (C). (D) Depth-cued representation (bright regions appear closest to the viewer) of Cabb-B overlaid with a $T = 7 /$ (left-handed) icosahedral lattice net. The net intersects at points that identify the positions of 72 capsomers, 12 of which occur at pentavalent locations and 60 of which occur at hexavalent locations.

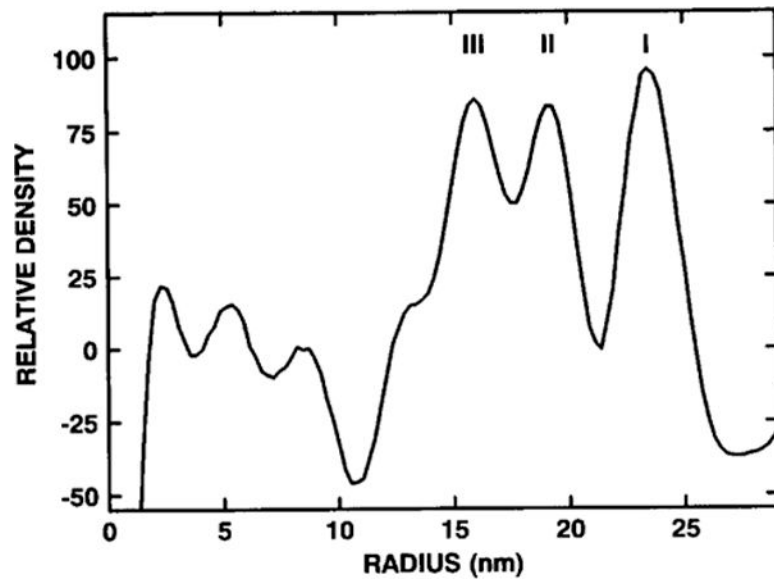


Fig. 5.

Radial density plot of the combined, spherically averaged Cabb-B and CM1841 reconstructions depicts the three concentric-layer (I, II, III) CaMV structure. Three major peaks occur at radii of 23.5 nm (I), 19.1 nm (II), and 16.0 nm (III). The layers extend from a minimum radius of ~ 12 nm to a maximum radius of ~ 26 nm, with most of the density confined within the outermost 10 nm. Density at $r < 11$ nm mainly corresponds to the solvent-filled central cavity.

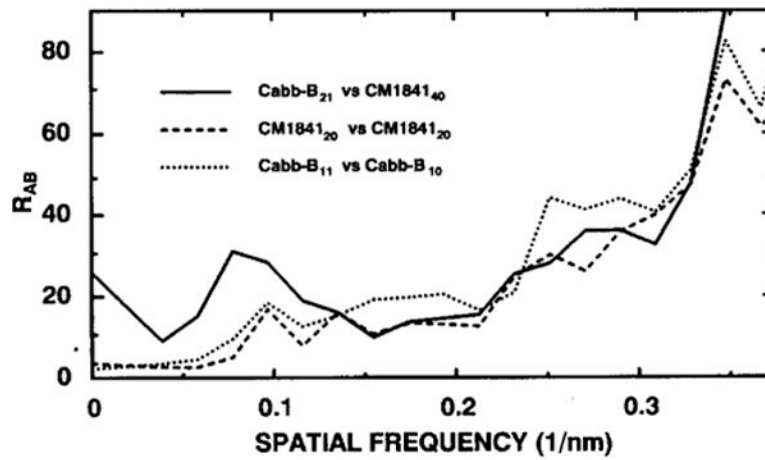


Fig. 6. Reliability index (R_{AB}) comparisons between independently refined and reconstructed subsets of Cabb-B (10 vs 11 particles) and CM1841 (20 vs 20) data and between the complete reconstructions of Cabb-B and CM1841 (21 vs 40). R_{AB} , plotted as a function of spatial frequency, shows excellent reliability within each of the individual data sets as well as excellent agreement between the full reconstructions to $\sim 0.34 \text{ nm}^{-1}$.

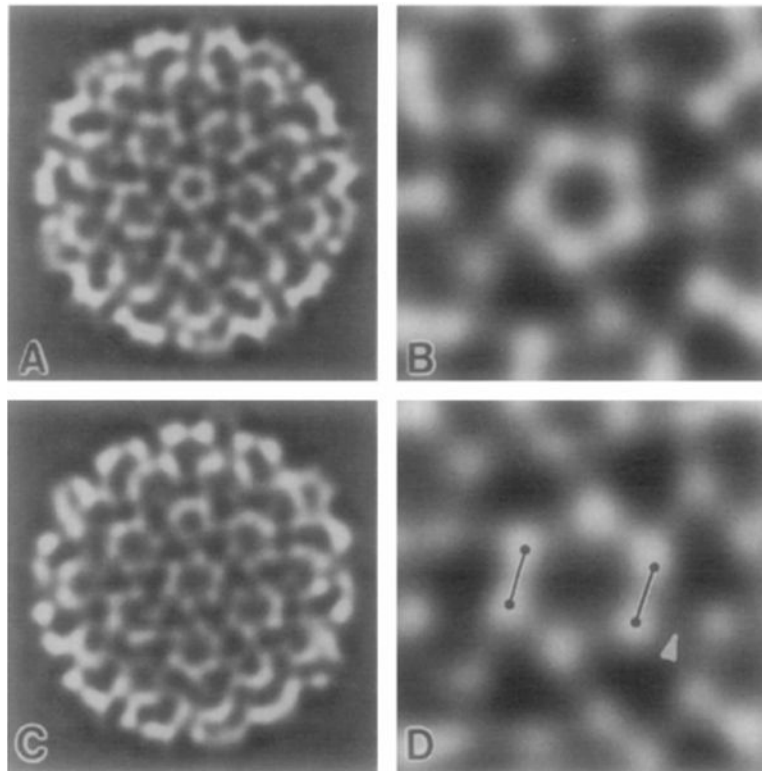


Fig. 7. (A) Half-particle, projected image of the density of layer I ($r = 21.2\text{--}26.9$ nm) from the Cabb-B reconstruction, viewed along the axis of the pentavalent capsomer. (B) Magnified view of the central region of (A) showing the regular substructure of the pentameric capsomer (dia. ~ 8.3 nm). (C) Same as (A) for a view along the axis of the hexavalent capsomer. (D) Magnified view of the central region of (C) showing the distorted substructure of the hexameric capsomer (maximum dia. ~ 10.3 nm). Symbols identify subunit-subunit interactions that are described under Results.

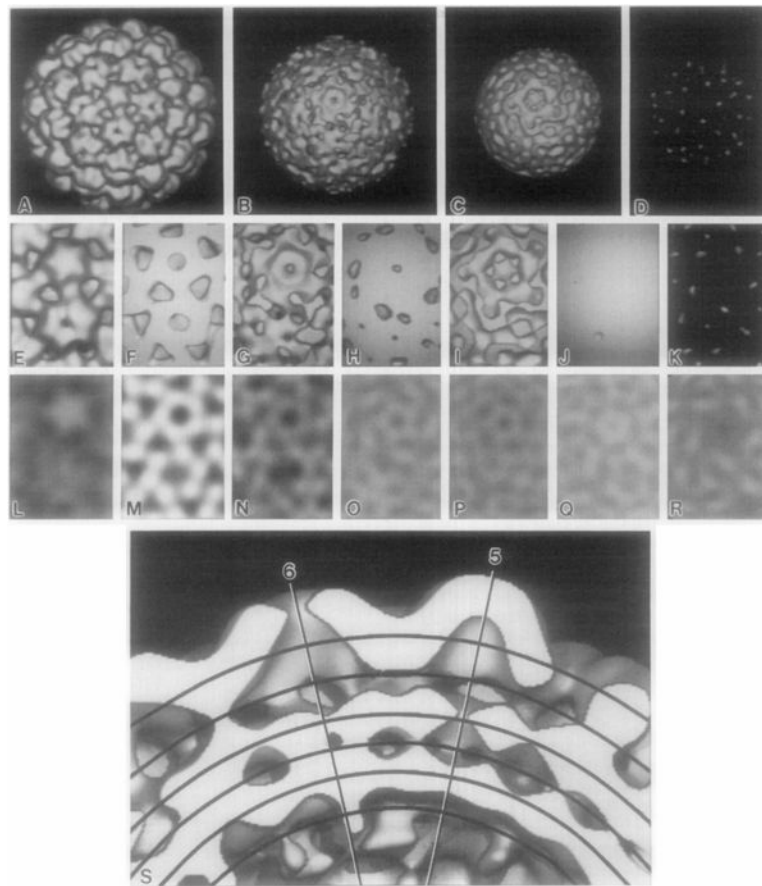


Fig. 8. The CaMV Cabb-B reconstruction presented as surface-shaded views, truncated at progressively lower radii (A–D and E–K), and as projected views of the density at specific radii (L–R). All these representations (A–R) are viewed along a radial direction midway between the axes of the pentavalent (toward the top) and hexavalent (toward the bottom) capsomer axes. A cutaway surface representation (S), in which only the left half of (A) is viewed from the right, reveals the internal features of the multilayer CaMV structure. Circular arcs mark the positions of peaks and troughs seen in the radial density plot (Fig. 5). These are at $r = 23.5$ (F,M), 21.2 (B,G,N), 19.1 (H,O), 17.6 (C,I,P), 16.0 (J,Q), and 14.5 nm (D,K,R). The reconstructed density along each of the circular arcs in (S) from right to left corresponds to the density along a central, vertical line in each of the panels in (E–R) from top to bottom.

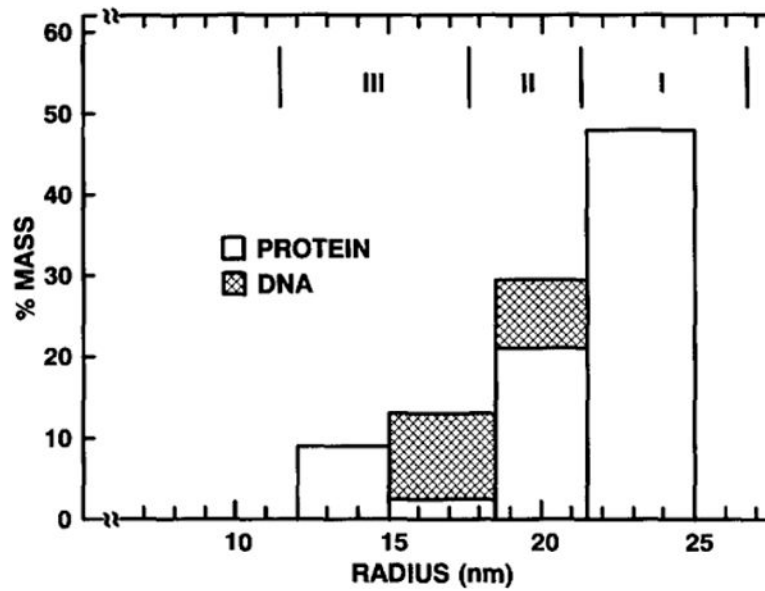


Fig. 9.

Comparison of multilayer models based on our image reconstructions and the neutron scattering experiments of Kruse et al. (1987). The three layers in the reconstruction model span radii of 21.2–26.9 nm (I), 17.6–21.2 nm (II), and 11.4–17.6 nm (III), whereas the neutron model is depicted with four layers that span radii of 21.5–25.0 nm, 18.5–21.5 nm, 15.0–18.5 nm, and 12.0–15.0 nm (Note: Kruse et al. (1987) label these respective layers IV, III, II, and I, whereas we use an opposite convention).